Table 1. Structural data and zero-pressure bulk moduli (B_0) for modified fluorite structures. Experimental data for SnO_2, RuO_2, PbO_2, and PdF_2 were obtained at 48, 8.9, 9.0, and 0.001 GPa, respectively. Theoretical values are those calculated for zero pressure.

Compound	a (Å)	u	B_0* (GPa)	Ref.
		Experimental		
SnO_2	4.8700(2)	0.347(1)	261(14)	†
RuO_2	4.8320(3)	0.347(1)	399‡	†
PbO_2	5.2804(3)	0.332(2)	223(9)	†
PdF_2	5.329(1)	0.3431(4)	§	(*12*)
		Theoretical		
SiO_2	4.40	0.3446	393	(*9*)
SiO_2	4.47	0.344	335	(*11*)
SiO_2	4.41	0.3349	363	(*20*)
SiO_2	4.55	0.337	348.5	(*21*)
SiO_2	4.43	0.344	347	(*21, 22*)
SiO_2	4.41	0.347	387	(*23*)
SiO_2	4.462	0.3445	312	(*24*)
GeO_2	4.643	0.3435	357	(*9*)

*B_0 values were obtained with the Birch-Murnaghan or Murnaghan equations of state (*25*) with first-derivative values between 3.5 and 7 for the experimental data and between 1.6 and 4.4 for the theoretical data. †From the present study. ‡From (*3*). §Not measured.

the fluorite structure assumed previously. The transition to the modified structure corresponds to an increase in cation coordination number from 6 to 6+2 instead of from 6 to 8. There are no remaining examples of a pressure-induced rutile-to-fluorite phase transformation. This represents an important modification to the structural systematics of metal dioxides. The fluorite structure adopted by many compounds under ambient conditions and at high temperatures is not a good candidate for a high-pressure structure because of the empty cubic site at the center of the unit cell. The present observation of transitions in SnO_2, RuO_2, and PbO_2 at high pressures to the $Pa\bar{3}$ structure reconciles the experimental behavior of these metal dioxides with the theoretical predictions for SiO_2 and GeO_2, yielding a common cubic high-pressure structure for these compounds.

REFERENCES AND NOTES

1. L. Liu and W. A. Bassett, *Elements, Oxides and Silicates* (Oxford Univ. Press, New York, 1986).
2. L. C. Ming and M. H. Manghnani, in *High-Pressure Research in Geophysics*, S. Akimoto and M. H. Manghnani, Eds. (Center Academic, Tokyo, 1982), pp. 329–347.
3. J. Haines and J. M. Léger, *Phys. Rev. B.* **48**, 13344 (1993).
4. W. B. White, F. Dachille, R. Roy, *J. Am. Ceram. Soc.* **44**, 170 (1961).
5. L. Liu, *Phys. Earth Planet. Inter.* **9**, 338 (1974).
6. ———, *Science* **199**, 422 (1978).
7. Y. Syono and S. Akimoto, *Mater. Res. Bull.* **3**, 153 (1968).
8. R. E. Cohen, in *High-Pressure Research: Application to Earth and Planetary Sciences*, M. H. Manghnani and Y. Syono, Eds. (American Geophysical Union, Washington, DC, 1992), pp. 425–431.
9. L. H. Jolly, B. Silvi, P. d'Arco, *Eur. J. Mineral.* **6**, 7 (1994).
10. Y. Tsuchida and T. Yagi, *Nature* **340**, 217 (1989); K. J. Kingma, R. E. Cohen, R. J. Hemley, H. K. Mao, *ibid.* **374**, 343 (1995).
11. K. T. Park, K. Terakura, Y. Matsui, *ibid.* **336**, 670 (1988).
12. A. Tressaud, J. L. Soubeyroux, H. Touhara, G. Demazeau, F. Langlais, *Mater. Res. Bull.* **16**, 207 (1981).
13. A. Tressaud and G. Demazeau, *High Temp. High Pressures* **16**, 303 (1984).
14. H. K. Mao, P. M. Bell, J. W. Shaner, D. J. Steinberg, *J. Appl. Phys.* **49**, 3276 (1978).
15. J. Rodríguez-Carvajal, paper presented at the 1990 Satellite Meeting on Powder Diffraction (XV Conference of the International Union of Crystallography), Toulouse, 16 to 18 July, 1990, p. 127.
16. K. Suito, N. Kawai, Y. Masuda, *Mater. Res. Bull.* **10**, 677 (1975); S. Endo *et al.*, *High Pressure Res.* **4**, 408 (1990).
17. R. M. Hazen and L. W. Finger, *J. Phys. Chem. Solids* **42**, 143 (1981).
18. J. Haines, J. M. Léger, A. Atouf, in *High Pressure in Material Science and Geoscience. Proceedings of the XXXII Meeting of the European High Pressure Research Group*, Brno, 29 August to 1 September 1994, J. Kamarád, Z. Arnold, A. Kapička, Eds. (Prometheus, Brno, 1994), pp. 133–136.
19. R. W. G. Wyckoff, *Crystal Structures* (Interscience, New York, 1951), vol. I, chap. IV; A. F. Wells, *Structural Inorganic Chemistry* (Oxford Univ. Press, Oxford, ed. 3, 1962), pp. 408, 512, and 520–523.
20. Y. Matsui and M. Matsui, in *Structural and Magnetic Phase Transitions in Minerals, Advances in Physical Geochemistry*, S. Ghose, E. Salje, J. M. D. Coey, Eds. (Springer, New York, 1988), pp. 129–140.
21. N. R. Keskar and J. R. Chelikowski, *Phys. Res. B* **46**, 1 (1992).
22. J. R. Chelikowski, N. Binggeli, N. R. Keskar, *J. Alloys Comp.* **197**, 137 (1993).
23. D. M. Sherman, *J. Geophys. Res.* **98**, 11865 (1993).
24. J. S. Tse, D. D. Klug, D. C. Allan, *Phys. Rev. B* **51**, 16392 (1995).
25. F. Birch, *J. Geophys. Res.* **57**, 227 (1952).

10 October 1995; accepted 7 December 1995

Large-Scale Storms in Saturn's Atmosphere During 1994

A. Sanchez-Lavega, J. Lecacheux, J. M. Gomez, F. Colas, P. Laques, K. Noll, D. Gilmore, I. Miyazaki, D. Parker

Large-scale storms are rarely observed in Saturn's atmosphere, but their appearance traces the wind velocity field, providing information on the vertical structure of the clouds and on the dynamics of the atmosphere. Two large-scale atmospheric disturbances formed by clouds highly reflective in the visible part of the spectrum were observed on Saturn during 1994. An equatorial disturbance with a longitudinal size of ~27,000 kilometers drifted in longitude with a velocity of 273.6 meters per second. A second disturbance, a rapidly evolving convective storm with an initial size ~7000 kilometers, was observed at 56 degrees south, moving with a zonal velocity of 15.5 meters per second.

Cloud systems with enough size and reflectivity contrast to be detected by ground-based telescopes are rare in Saturn's atmosphere (*1–3*). Only five large-scale atmospheric disturbances at different latitudes between 5° and 60°N, known as Great White Spots (GWSs) (*1, 2, 4–9*) and spaced in time by ~30 years, have been observed in the visible part of the electromagnetic spectrum during the last century. The equatorial disturbances (GWS 1876, 1933, and 1990) were characterized by an initial single outburst of bright white clouds (size ≈20,000 km) that showed divergent motions (suggestive of a vigorous upward convection process). After the first 2 weeks of their lives, these GWSs expanded zonally (east-west), with the bright clouds moving away along the parallels, in accordance with the local wind velocity. Once these clouds had encircled the planet (taking about 1 month for the equatorial events), their morphology, occupying a latitude band of about 15°, was formed by a wavy pattern of smaller scale white spots spaced quasi-regularly (size ≈5000 km and lifetime <10 days for these spots). The decay of this activity took place over a few months, during which the patterns lost contrast and the clouds dissipated (*2, 5–7*). The last GWS was observed at the equator in 1990 (*6–9*). After this last disturbance, synoptic-scale short-lived cloud formation occurred in the equatorial region of Saturn during 1991 (*10*), 1992, and 1993.

Here, we report on two disturbances observed at different latitudes during the second half of 1994 (*11, 12*). Most of the images were taken with a CCD (charge-coupled device) camera installed on the dedicated 1-m planetary telescope at Pic-du-

A. Sanchez-Lavega, Departamento de Física Aplicada I, Escuelo Tecnica Superior Ingenieros, Universidad Pais Vasco, Alda. Urquijo s/n, 48013 Bilbao, Spain.
J. Lecacheux, Department des Recherches Spatiales, Observatoire Meudon, 92195 Meudon, France.
J. M. Gomez, Grup Estudis Astronomics, Apartado 9481, 08080 Barcelona, Spain.
F. Colas, Bureau des Longitudes, 77 Avenue Denfert Rochereau, 75014 Paris, France.
P. Laques, Observatoire Pic-du-Midi, 65200 Bagneres de Bigorre, France.
K. Noll and D. Gilmore, Space Telescope Science Institute, 3700 San Martin Drive, Baltimore, MD 21218, USA.
I. Miyazaki, Oriental Astronomical Association, Naha-shi, Okinawa, Japan.
D. Parker, Association of Lunar and Planetary Observers, Coral Gables, FL 33156, USA.

Midi Observatory in the French Pyrenees, with a set of filters covering the wavelength range from 0.48 to 1.0 μm (Table 1). These observations were augmented by images taken with 0.4-m telescopes in Florida (United States), Japan, and Spain that were also equipped with CCD cameras. With these facilities we observed Saturn during 62 nights between 6 June and 17 December 1994 (*13*). The equatorial storm was also imaged in the near infrared (2.0 to 2.14 μm, with a circular variable filter) on 8 September at the National Aeronautics and Space Administration (NASA) Infrared Telescope Facility (IRTF) with a 3-m telescope and an InSb 256 pixel by 256 pixel array. We also used high-resolution images of the equatorial storm obtained during one orbit by the Hubble Space Telescope (HST) on 1 December, taken with various filters in the wavelength range 0.255 to 0.953 μm.

Our first observation of major, white-cloud activity in the equatorial region (planetographic latitudes 8° to 10°N) occurred on 19 July. The cloud morphology in this region (Fig. 1, A through D, and Fig. 2) consisted of a small white spot (W1) followed about 40° to the west by the main storm (WS, oval shape, size ≈15°), separated by about 23° from an elongated dark feature further to the west (DS, size ≈15°), which was followed by another small white spot (W2) about 37° away. By the end of August, an antipodal large spot (AS) (similar in size to WS) had formed ~180° from WS (Fig. 1D). The disturbance reached its maximum degree of activity and manifested itself as a cloud pattern (from east to west: W1, WS, DS, W2, and AS, together with other minor and transient scattered spots located between them) spanning latitudes ~3° to 27°N.

Table 1. Spectral characteristics of the observations. Abbreviations: PIC, Pic-du-Midi Observatory; λ_{eff} and $\delta\lambda$, effective filter wavelength and passband [major absorption gases (CH_4 and H_2) or isolated continuum (cont) are indicated when appropriate; n and N mean narrow interference filters; M, medium; W, wide; B, blue; V, visual; R, red; I, infrared; p, partial absorption]; P_R, pressure level at which the optical depth attributed to Rayleigh scattering by the gas is 1; and P_{abs}, pressure level at which the optical depth attributed to gas absorption is 1. Particle sensitivity: cloud and haze levels sensed according to standard models of Saturn's upper vertical distribution of particles (*20*); strat., stratospheric; tropo., tropospheric.

Obs.	λ_{eff} (nm)	$\delta\lambda$ (nm)	P_R (bar)	P_{abs} (bar)	Particle sensitivity
HST	261 (F255W)	42	0.140	–	Strat. and trop. hazes
HST	336 (F336W)	40	0.580	–	Strat. and trop. hazes
HST	410 (F410M)	15	0.942	–	Strat. and trop. hazes
PIC	480 (B)	80	2.04	–	Trop. haze, upper NH_3 cloud
PIC	514 n	9.1	2.7	–	Trop. haze, upper NH_3 cloud
PIC	580 (V)	140	>5	–	Trop. haze, upper NH_3 cloud
PIC	650 (R)	140	>5	–	Trop. haze, upper NH_3 cloud
HST	673 (F673N)	4.7	>5	–	Trop. haze, upper NH_3 cloud
PIC	605 (cont) n	4	5.1	–	Trop. haze, upper NH_3 cloud
PIC	619 (CH_4) n	2	–	4.7	Trop. haze, upper NH_3 cloud
PIC	725 (CH_4) n	1.8	–	0.71	Trop. haze
PIC	751 (cont) n	5.0	>10	–	Trop. haze, upper NH_3 cloud
PIC	829 (cont) n	4.6	>10	–	Trop. haze, upper NH_3 cloud
PIC	860 (I)	200	>10	0.2	Strat. and trop. hazes
PIC	893 (CH_4) n	4.5	–	0.19	Strat. and trop. hazes
HST	888 ($FQCH_4$) n	14.6	–	0.19	Strat. and trop. hazes
HST	953 (F953N)	6.73	>10	–	Trop. haze, upper NH_3 cloud
IRTF	2000 (cont)	60	5–10	–	Trop. haze, upper NH_3 cloud
IRTF	2040 (CH_4 p)	60	–	2.5	Trop. haze, upper NH_3 cloud
IRTF	2070 (H_2)	60	–	0.3	Trop. haze
IRTF	2100 (H_2)	64	–	0.05–0.1	Strat. haze
IRTF	2140 (CH_4+H_2)	64	–	0.03–0.05	Strat. haze

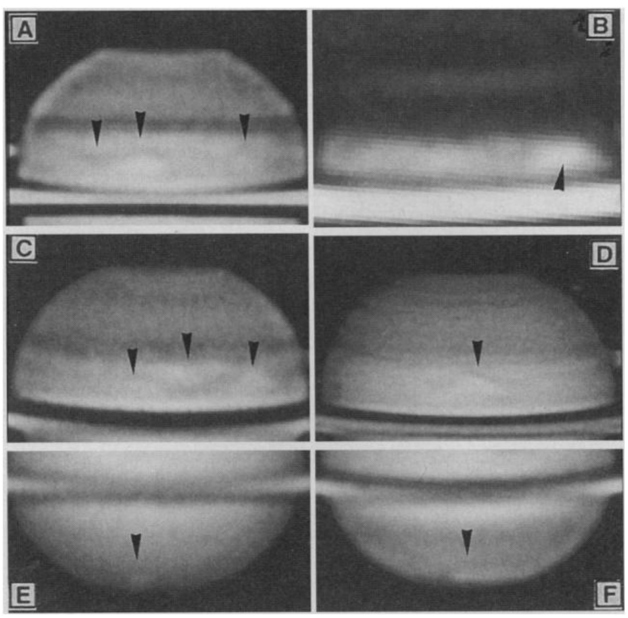

Fig. 1. Ground-based images of disturbances in Saturn's atmosphere in 1994. (**A** through **D**) The northern equatorial storm: (A) 28 July (arrows indicate, from left to right, DS, WS, and W1); (B) 8 September (arrow marks WS, close to east limb); (C) 20 November (arrows indicate, from left to right, W2, the white cloud channel, and WS); and (D) 22 November (arrow indicates AS). (**E** and **F**) The southern subpolar disturbance: (E) 13 August (arrow marks initial storm) and (F) 2 September (arrow marks main storm and eastward expansion of the clouds). North is up and east is to the right in all the images. All images were taken with Pic filter I, except for (B), which was taken at 2140 nm by IRTF.

The WS and AS were the most prominent features, especially from October to December when the other features were nearly undetectable from Earth. Both features had a triangular shape. The base of WS was ~27,000 km wide at 5°N, and its vertex was at 20°N, such that WS had a meridional width of ~12,000 km. Beginning in September, a white channel of clouds spread more than 30° west from the WS vertex. This spreading of the WS vertex was observed 3 months later by the HST (Fig. 2). Contrast-enhancement processing of these images by an unsharp mask (*13*) showed the internal structure of the WS with some detail: two narrow bands, one tilted east and the other tilted west (length ~17,000 km, width ~1500 km), enclosed a core area (size ~6500 km). The latitudinal wind shear sculpted these forms, with the white channel at 20°N being formed by clouds dragged westward from the storm vertex, flowing around the DS, which acted as a barrier to this flow.

The zonal (east-west) velocities of these features were measured relative to Saturn's System III rotation rate (*14*) by cloud tracking. All features moved uniformly during the observing period: the WS, centered at 9.4° ± 1.0°N, had a zonal velocity u = 273.6 ± 2.5 m s^{-1} for 51 nights between 15 July and 16 December, and the AS at 11.3° ± 1.4°N had u = 281.8 ± 1.2 m s^{-1} for 11 nights between 27 August and 17 December. The other features at similar latitudes (W1, DS, W2, and three smaller spots) ranged in zonal velocities from 269 to 282 m s^{-1}. Cloud tracking of short-lived, small-scale spots between 18° and 20°N showed that at these latitudes u = 243.9 ± 4.6 m s^{-1}, indicating a decrease of the zonal wind velocity with increasing latitude, indicating a cyclonic vorticity for the meridional wind shear at these latitudes. The WS and AS, as well as the other features at the same latitudes, moved at speeds 100 to 150 m s^{-1} slower than the wind speeds measured by

Voyager in 1981 (3) (Fig. 3A), indicating a decrease in zonal winds at the higher altitude of the storm's clouds. A large seasonal (radiative) change in the equatorial winds or their dynamical forcing after the 1990 GWS may also have contributed to this decrease (15). An alternative explanation is that the relative drift of the disturbance represents the westward phase propagation of a wave relative to the local flow (16).

Because we imaged WS from ultraviolet to near-infrared wavelengths (including several CH_4 absorption bands) (Figs. 1B and 2), spectral reflectivity measurements as a function of scattering angles allowed analysis of the storm's vertical cloud structure (Table 1). The planet reflectivity was calibrated with recently measured reflectivities for Saturn (17). A simple radiative transfer model that included Rayleigh scattering by an H_2-He mixture and absorption by CH_4 above a Lambertian semi-infinite cloud with a wavelength-dependent reflectivity (18) allowed us to locate the cloud tops at atmospheric pressure $P = 50 \pm 15$ mbar. Similar results were obtained with a semi-infinite isotropic cloud instead of a Lambert cloud base. This altitude is two scale heights (19) above the visible cloud tops at ~400 mbar or 3.5 scale heights above the main NH_3 cloud deck at 1.8 bar (20). The high location of the cloud tops is consistent with the lower zonal velocity measured for the WS and other features if the zonal wind velocity decreases by ~50 to 75 m s^{-1} per scale height (21). The low reflectivity of the storm in the ultraviolet (0.255 and 0.355 μm) coupled with the high reflectivity at wavelengths longer than 0.41 μm indicates that the cloud particles that formed the storm were more absorbent at short wavelengths [single-scattering albedo (22) $\varpi_0 \sim 0.4$ at 0.255 μm, $\varpi_0 \sim 0.7$ at 0.355 μm, and $\varpi_0 \sim 0.75$ at 0.410 μm] but brighter at longer wavelengths ($\varpi_0 > 0.95$ at wavelengths >0.48 μm) when compared with Saturn's normal clouds.

According to our images, the 1994 event does not fit into the classical GWS cloud pattern (2, 4–9). The compactness, size, and persistence of the WS (it was tiny but still visible in May 1995, at an age of >11 months) against wind shear (which will destroy cloud patterns in a few days) were unique among the equatorial GWS disturbances, suggesting that WS was a coherent, dynamically stable structure. We have no evidence of convergent or divergent motions within the WS, and the cloud morphology was not consistent with a closed vortex (no rotation was observed). This disturbance may have been a major manifestation at high altitudes (minor events could be those observed from 1991 to 1993) of an instability in the equatorial atmosphere that remained after the 1990 GWS.

A second, unrelated disturbance was observed in the southern hemisphere on 13 August (12). Initially it was a round white spot ~7000 km in diameter, centered at 56°S but with an enlarged white appendage of ~4500 km in the northeastern extremity at 53°S (Fig. 1E). This appendage represents the expansion of the white clouds by the prevailing zonal winds at this latitude (Fig. 1F). Cloud tracking of the initial white spot (12 nights between 13 August and 1 December) gave a zonal velocity $u = 15.5 \pm 2.0$ m s^{-1} at a latitude 56.5° ± 2.2°S. White clouds expanded eastward at $u = 30 \pm 4$ m s^{-1} in a latitude band between 50° and 61°S. Both values are similar (Fig. 3B) to those derived from Voyager images taken during 1980 and 1981 (3) and to an isolated, long-lived feature observed from 1969 to 1971 (23). The HST observations on 1 December in the 0.89-μm CH_4 band revealed a series of dark spots each ~2000

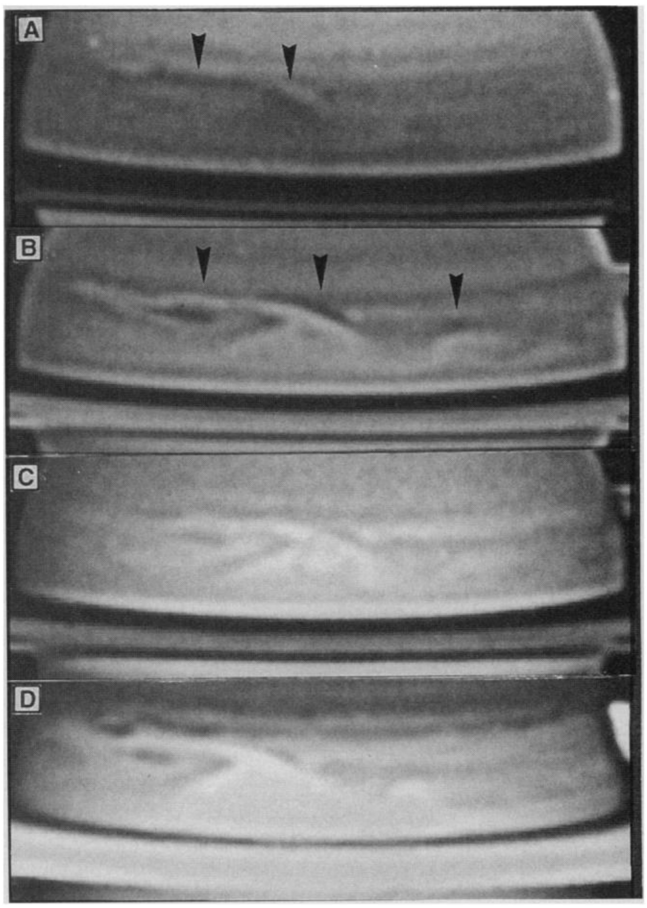

Fig. 2. Mosaic of HST images of the northern equatorial storm taken through different filters on 1 December. Each strip covers a latitude band from 2°S (above the rings) to 32°N. Wavelengths: (**A**) 261 nm, (**B**) 410 nm, (**C**) 673 nm, and (**D**) 888 nm (CH_4 band, saturated in the storm). Features (arrows) in (A) and (B) are (left to right) DS and (northwards, surrounding it) the white cloud channel, main storm WS, and feature W1. Compare the reflectivity reversal of the storm features in the continuum from the ultraviolet (A) to the blue (B) and red (C) images.

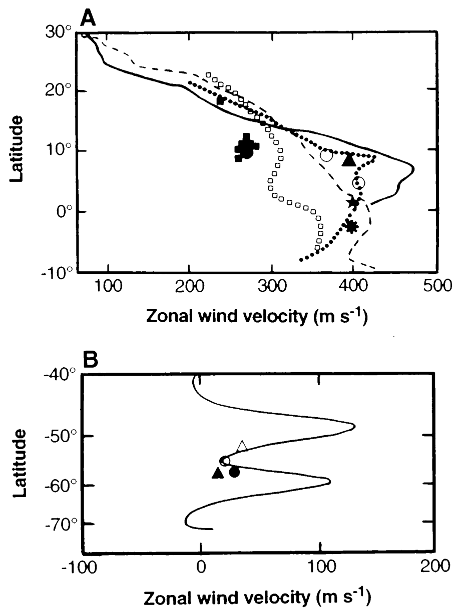

Fig. 3. (**A**) Zonal wind velocity profile in the equatorial region from Voyager 2 data (3) (solid line); 1990 and 1991 Pic-du-Midi data (6, 10) (dotted line); 1990 HST 547-nm data (8) (dashed line); and 1990 HST 890-nm CH_4-band filter data (8) (open squares). Single points mark large-scale storms: GWS 1876 (2) (triangle); GWS 1933 (2) (star); GWS 1990 (open circle), which showed two motions in time (6); and two long-lived spots in 1991 (10) (asterisk). The features from 1994: WS (solid circle) and W1, W2, DS, AS, and smaller spots (solid squares), including those at 20°N. (**B**) Zonal wind velocity profile in the southern hemisphere from Voyager 2 data (3) (line); the Anne spot (open circle), which was a vortex observed by Voyager 1 and 2 in 1980 and 1981 (3); a long-lived spot observed from 1969 to 1971 (23) (solid circle); the core of the 1994 storm (solid triangle); and the average velocity of the eastward expansion of this storm (open triangle).

to 3000 km wide separated regularly by ~6800 km alongside a dark belt at 50°S that probably pertained to a wave phenomena resulting from the disturbance. The morphologic evolution of this disturbance resembled, on a smaller scale, previous GWS disturbances (5), and it was probably a transient convective phenomenon rapidly dispersed by the zonal winds.

This observation, together with other transient spots observed in recent times (10), suggests that mid-scale storms on Saturn could be more frequent than previously thought. Their detection is a question of the temporal coverage of the observations, the techniques used, and the contrast of the features against the background of normal clouds.

REFERENCES AND NOTES

1. A. F. Alexander, *The Planet Saturn* (Faber and Faber, London, 1962).
2. A. Sanchez-Lavega, *Icarus* **44**, 1 (1982).
3. A. P. Ingersoll, R. F. Beebe, B. J. Conrath, G. E. Hunt, in *Saturn*, T. Gehrels and M. S. Matthews, Eds. (Univ. of Arizona Press, Tucson, 1984), pp. 195–238.
4. A. Sanchez-Lavega and E. Battaner, *Astron. Astrophys.* **185**, 315 (1987).
5. A. Sanchez-Lavega, *Chaos* **4**, 341 (1994).
6. A. Sanchez-Lavega *et al.*, *Nature* **353**, 397 (1991).
7. R. F. Beebe, C. D. Barnet, P. V Sada, A. S. Murrel, *Icarus* **96**, 163 (1992).
8. C. D. Barnet, J. A. Westphal, R. F. Beebe, L. F. Huber, *ibid.* **100**, 499 (1992).
9. J. A. Westphal *et al.*, *ibid.*, p. 485.
10. A. Sanchez-Lavega, J. Lecacheux, F. Colas, P. Laques, *J. Geophys. Res.* **98**, 18857 (1993).
11. A. Sanchez-Lavega, J. M. Gomez, J. Lecacheux, F. Colas, I. Miyazaki, *IAU Circ. No. 6079* (1994).
12. J. M. Gomez, J. Caquel, P. Laques, *IAU Circ. No. 6059* (1994).
13. Most images were taken through filter I (Table 1), which is sensitive to high-altitude hazes. Image processing methods were similar to those described by A. Sanchez-Lavega, J. Lecacheux, F. Colas, and P. Laques [*Science* **260**, 329 (1993)]. For morphology studies, we used an unsharp-mask image processing technique that consists of creating a degraded image from the original one and making an intermediate image from their subtraction. Using some calibration constants, it is possible to obtain a final image that is well contrasted on all parts of the planetary disk up to its edges. This treatment is efficient in discriminating fine features of low contrast.
14. Longitudes and zonal wind velocities are measured relative to the System III rotation rate (period = 10 hours and 39.4 min), which is presumed to be that of the planet's magnetic field linked to the planet's interior [M. D. Desch and M. L. Kaiser, *Geophys. Res. Lett.* **8**, 253 (1981)].
15. A seasonal radiative-dynamic model of Saturn's troposphere suggests temporal changes in wind speeds within the equatorial region (30°N to 30°S), mainly as a result of ring shadowing and Saturn's tilt [C. D. Barnet, R. F. Beebe, B. J. Conrath, *Icarus* **98**, 94 (1992)].
16. These spots could be the manifestation of a planetary Rossby wave. There are at least two well-known examples of waves in Saturn's atmosphere that could be of this type: the polar hexagon [D. A. Godfrey, *Icarus* **76**, 335 (1988); M. Allison, D. A. Godfrey, R. F. Beebe, *Science* **247**, 1061 (1990)] and the ribbon wave [L. A. Sromovsky, H. E. Revercomb, R. J. Krauss, V. E. Suomi, *J. Geophys. Res.* **88**, 8650 (1983)]. In its simplest form, the long-wave phase velocity of a Rossby wave can be estimated as $c = -\beta_0 L_R^2$ [G. P. Williams and T. Yamagata, *J. Atmos. Sci.* **41**, 453 (1984)], where $\beta_0 = 2\Omega(\cos\varphi_0)/R$ is the planetary vorticity gradient and $L_R = (gH)^{1/2}/f_0$ is the Rossby deformation radius. Here $\Omega = 1.638 \times 10^{-4}$ rad s^{-1} is the planetary angular velocity, $\varphi_0 = 9$°N is the latitude, $R = 60{,}200$ km is the distance from the center of the planet, g is the acceleration due to gravity, $f_0 = 2\Omega(\sin\varphi_0)$ is the Coriolis parameter, and H is a characteristic vertical scale in the atmosphere. With the above values, $\beta_0 = 5.4 \times 10^{-12}$ m^{-1} s^{-1}, and c between -100 and -150 m s^{-1}, we get $L_R =$ 4300 to 5250 km, corresponding to a wavelength $2\pi L_R =$ 27,000 to 33,000 km, comparable with the longitudinal size of WS.
17. Standard photometric reduction procedures were applied to the Pic-du-Midi images. Flux calibration in the 300- to 1000-nm spectral region was performed on a beam 2 arc sec in diameter on the center of the disk with the use of recently measured reflectivities [E. Karkoschka and M. G. Tomasko, *Icarus* **106**, 428 (1993); E. Karkoschka, *ibid.* **111**, 174 (1994)]. For the 261-nm filter, we used absolute reflectivity measurements presented by R. A. West *et al.* [*J. Geophys. Res.* **88**, 8679 (1983)]. In the 2000- to 2140-nm spectral range, we used the absolute reflectivities of R. N. Clark and T. B. McCord [*Icarus* **40**, 180 (1979)].
18. A. Sanchez-Lavega, J. Lecacheux, F. Colas, P. Laques, *Icarus* **108**, 158 (1994). A Lambert surface of reflectivity A is one that reflects A times the flux incident on it in such a way that the reflected intensity is independent of the direction to the observer.
19. The scale height is defined as $H = RT/\mu g$, where R is the gas constant, T is the temperature, and μ is the mean molecular weight of the atmosphere. In Saturn's troposphere, $H \approx 45$ km. The tracers used to measure the Voyager velocities are assumed to have been measured at an average pressure of 400 mbar (*20*).
20. M. G. Tomasko, R. A. West, G. S. Orton, V. G. Tejfel, in *Saturn*, T. Gehrels and M. S. Matthews, Eds. (Univ. of Arizona Press, Tucson, 1984), pp. 150–194; E. Karkoshka and M. G. Tomasko, *Icarus* **97**, 161 (1992).
21. There are different observations that suggest that globally the zonal wind velocity decreases with height on Saturn: (i) Atmospheric temperatures at and above the cloud deck (pressure levels of 150, 290, and 730 mbar) derived from Voyager Infrared Interferometer Spectrometer (IRIS) measurements and the thermal-wind relation suggest an averaged vertical wind shear of ~20 m s^{-1} per scale height [B. J. Conrath and J. A. Pirraglia, *Icarus* **53**, 286 (1983)]. However, an exception was the equatorial region (10° to 25°N), where the eastward equatorial jet increases in speed with height according to this analysis. (ii) On the contrary, HST wind speeds derived from cloud tracking of the equatorial 1990 GWS at two levels (~100 and 300 mbar) gave a zonal wind that decreases by ~45 m s^{-1} per scale height in the latitude range 0° to 10°N (*8*), closer to our results.
22. The single-scattering albedo ϖ_0 is the ratio of the particle's cross section for scattering to the sum of its cross sections for scattering and absorption (ϖ_0 = 1 for purely scattering particles, ϖ_0 = 0 for absorbing particles). The origin for the short-wavelength absorption is unknown, but an ultraviolet-blue aerosol agent must be mixed with the NH_3 ice particles that presumably form the disturbance clouds.
23. E. J. Reese, *Icarus* **15**, 466 (1971).

24. We thank R. Beebe for initiating the HST Director's Discretionary Observation of the 1994 Saturn storm as a service to the community, J. R. Acarreta for the radiative-transfer calculations, and two anonymous reviewers for helpful comments. K.N. was a visiting astronomer at the IRTF, operated by the University of Hawaii under contract from NASA. This work was supported by Universidad Pais Vasco (grant EA054/95) and the French National Programme of Planetology.

12 September 1995; accepted 6 December 1995

Group Velocity in Strongly Scattering Media

J. H. Page,* Ping Sheng, H. P. Schriemer, I. Jones, Xiaodun Jing,† D. A. Weitz‡

Investigation of the ballistic propagation of acoustic waves through a resonantly scattering, inhomogeneous medium indicates that although the ballistic signal remains coherent with the incident pulse, it is nevertheless strongly affected by scattering resonances. These resonances cause considerable frequency dispersion and substantially reduce the phase and group velocities. The experimental data are quantitatively described by a theoretical model that correctly accounts for the coupling between the resonant scatterers, leading to an effective renormalization of the scattering within the medium. This approach resolves a long-standing problem in the definition of the group velocity in strongly scattering materials.

Virtually all forms of energy are propagated by waves: heat and sound in the form of acoustic waves, and radio and light in the form of electromagnetic waves. In any medium, wave propagation depends on the relation of the angular frequency of a wave, ω, to its wave vector, k, as given by the dispersion relation $\omega(k)$. Whenever the dispersion relation is nonlinear, waves of different frequencies travel at different speeds and typically require two distinct velocities to describe wave propagation: The first is the phase velocity, $v_p = \omega/k$, the speed at which a plane of constant phase propagates; the second is the group velocity, $v_g = d\omega(k)/dk$, normally the speed at which a pulse or signal propagates. However, the meaning of the group velocity is strictly well defined only when the dispersion of the medium is not too large (*1*). Nevertheless, even in a highly dispersive medium, a signal can still propagate, and the determination of its speed of propagation is a classic problem, having been recognized in the work of Sommerfeld (*2*) and Brillouin (*3*).

One important manifestation of this problem is the description of wave propagation through strongly scattering, inhomogeneous materials (*4*). In the intermediate-frequency regime, where the length scale of the inhomogeneities is comparable to the wavelength of the wave, the excitation of